

# Supporting Information for

## Free Energy Calculations on the Two Drug Binding Sites in the M2 Proton Channel

Ruo-Xu Gu<sup>†</sup>, Limin Angela Liu<sup>\*†</sup>, Dong-Qing Wei<sup>\*†</sup>, Jian-Guo Du<sup>‡</sup>, Lei Liu<sup>‡</sup> and Hong Liu<sup>‡</sup>

<sup>†</sup>State Key Laboratory of Microbial Metabolism (Shanghai Jiao Tong University), Luc Montagnier Biomedical Research Institute and College of Life Sciences and Biotechnology, Shanghai Jiao Tong University, Shanghai Minhang District, China 200240

<sup>‡</sup> Institute of Earthquake Science, China Earthquake Administration, Beijing, China 100036

**Review of the M2 Channel Structure and Function.** Viral matrix protein M2 embedded in the viral lipid envelope is described as a pH-activated proton channel<sup>1</sup> and believed to be crucial to the life cycle of the influenza virus.<sup>2, 3</sup> The channel is closed when the N-terminal environmental pH is greater than 8.5. The channel is believed to open when this pH value is about 6 and its conductance reaches saturation when this pH value is less than 4.<sup>1</sup> The type A influenza virus M2 channel (A/M2) is a homotetramer that is assembled by four 97-residue peptides in an N-out C-in arrangement across the viral lipid envelope.<sup>2, 3</sup> The transmembrane domain of the M2 channel is constituted by four parallel transmembrane helices forming a left-handed tetramer where each monomer contains 22 residues

(residue number 25 to 46 in Fig. S1A).<sup>4, 5</sup> The residues in the transmembrane domain are largely hydrophobic. Only five residues in the transmembrane domain are hydrophilic and believed to be critical in the proton conduction ability of the ion channel and they are: Ser31, Gly34, His37, Asp44, and Arg45. Gly34 was observed to lead to kinks in the otherwise straight transmembrane alpha-helix.<sup>6, 7</sup> His37 was shown to play a key role in proton transfer,<sup>2, 3</sup> although the exact proton conduction mechanism is still debatable.<sup>8-11</sup> Asp44 and Arg45 from adjacent helices were found to form salt bridges or hydrogen bonds that stabilize the homotetramer in the closed state of the channel.<sup>4</sup> Two hydrophobic residues, Val27 and Trp41, were found to orient toward the channel lumen, thereby occluding the pore and forming the channel gates at the N- and C- terminal ends of the M2 protein, respectively.<sup>4, 12, 13</sup>

**Support of the P-binding Site.** The pore-binding model has been believed to be the only possible drug binding site until recently. This model has a large number of experimental studies for support. For instance, the 1:1 drug to channel ratio in this structure is consistent with the experimental finding that amantadine was found to bind to the channel with a stoichiometry of 1:1 and a Hill coefficient of 0.91.<sup>14</sup> In addition, neutron diffraction studies showed that amantadine lies in the outer part of the membrane.<sup>15</sup> Moreover, mutant strains of M2 channel where the N-terminal part of the channel is mutated (such as L26F, V27A, A30T, S31N, and G34E) often lead to drug resistance,<sup>2, 3, 16, 17</sup> suggesting that the drug probably enters the channel from the N-terminal end and binds in the pore. A recent B/M2 and A/M2 chimera experiment also supports the P-binding model.<sup>13, 18</sup> Type B influenza virus M2 protein (B/M2) is not sensitive to rimantadine or amantadine. Chimeric M2 channel containing A/M2 protein's N-terminal part and B/M2's C-terminal part (replacing 6-18aa of B/M2 with 24-36aa of A/M2, with the transmembrane domain of B/M2 ranging from residue 6 to 27) was found to be sensitive to amantadine. Chimeric channel containing B/M2 protein's N-terminal part and A/M2's C-terminal part (replacing 19-27aa of B/M2 with 37-45aa of A/M2) was resistant to amantadine.

**Support of the S-binding Site.** Pielak et al. found that mutation of residues from the surface binding pocket (D44A, and L40A/I42A/L43A triple mutant) induced drug resistance.<sup>19</sup> These authors also found that the mutation S31N destabilized helical packing of the channel and destroyed the binding sites on the protein surface, resulting in drug resistance of the mutant.

**Simulation Protocols.** GROMACS 3.1.1<sup>20, 21</sup> was used for energy minimization and molecular dynamics simulations. The GROMOS united-atom force field parameters<sup>20</sup> for proteins and the force field parameters of Berger et al.<sup>22</sup> for lipid molecules were used. The structure of the rimantadine molecule was obtained from the solution NMR structure<sup>5</sup> and the parameter file was generated by the PRODRG package.<sup>23, 24</sup> The atom type and partial charge assignment of lipids and rimantadine are shown in Fig. S2. The protonation states of all titratable residues were determined using the software H++.<sup>25, 26</sup> At pH 7.5, the four His37 residues were found to be neutral in charge from our calculations as well as several previous studies.<sup>12, 27</sup> We assigned these residues to be singly-protonated at the delta position in accord with the solution NMR structure. Minimizations were first carried out on the solvated wild-type starting structures (500 steps, using steepest descent algorithm). Afterwards, molecular dynamics simulations were performed. Constraints were first applied to the protein, lipid, and drug molecules to allow the solvent to fully relax. Then constraints were slowly removed to allow the lipid and drug molecules to closely pack around the protein for 6 ns to allow the systems to reach equilibrium. Finally, unconstrained simulations were carried out for 15 ns for the wild-type. After 2 ns of production runs of the wild-type, the Ser31 residue was mutated to asparagine, and 13 ns simulations were carried out for the mutant. For all simulations, periodic boundary conditions were employed in all three dimensions. NPT ensemble (300 K, 1 atm) was used in all simulations using the Berendsen method (time constant 0.1 ps) and anisotropic scaling (time constant 1 ps) for temperature and pressure control, respectively. A 14 Å cut-off was used for van der Waals interactions. Particle mesh Ewald (PME) method was used for long range electrostatic interactions. The LINCS algorithm<sup>28</sup> was used to constrain all bonds in the systems. The time step was 2 fs.

**Potential of Mean Force Calculations.** Potential of mean force calculations were performed to obtain the free energy barriers and the binding energy changes associated with three binding reactions of rimantadine, including a rimantadine molecule binding to the M2 channel pore, to the C-terminal M2 channel surface, and to the lipid-water environment. Our PMF calculation methods are similar to those used in Chew et al.'s work.<sup>29</sup>

First, the potential of mean force (PMF) of a protonated rimantadine entering and binding in the channel pore from the solvent phase at the N-terminal end was calculated using umbrella sampling method (in short, P-binding PMF).<sup>30</sup> Ninety windows were employed. To ensure that the simulations of different windows were uncorrelated, ninety snapshots were randomly extracted from the last 5 ns simulations of the P-binding model. The original rimantadine molecule was removed and a new rimantadine molecule was placed in each snapshot with its mass center positioned along the channel axis from the N-terminal end of the channel to the vicinity of His37 at an interval (or window) of 0.33 Å. These structures serve as starting conformations at each window. Molecular dynamics simulations were then performed for 2 ns for each window. The first nanosecond was considered equilibration whereas the second nanosecond was analyzed in the energy profile calculation. A force constant of 4500 KJ/mol/nm<sup>2</sup> was applied on the drug's mass center to restrain it at its initial position. The force constant was chosen so that the positions of rimantadine's mass centers in adjacent windows had a fair amount of overlap. The MD simulation parameters were the same as those used in the "Simulation Protocols" section. The same PMF calculation was performed for both the wild-type and the S31N mutant.

Second, the PMF of rimantadine leaving the S-binding state to enter the lipid-water environment was computed (in short, S-binding PMF). Sixty windows were used. The initial structures of each window were extracted from the last 5 ns simulation of the S-binding form of the wild-type. Protonated rimantadine molecules were inserted into the water-lipid interfacial region from the S-binding site to the boundary of the simulation box along the Y axis of the membrane plane. These structures serve as

starting conformations at each window. MD simulations were then carried out in the same way as the P-binding free energy calculation discussed in the previous paragraph.

Third, the PMF of a protonated rimantadine passing through the DPPC bilayers was calculated (in short, L-binding PMF). A hundred and three windows were used in this calculation. First, MD simulation was performed on a pre-equilibrated DPPC bilayer<sup>31, 32</sup> for 5 ns. Then, a hundred and three snapshots were randomly extracted from the last 2 ns. Protonated rimantadine molecules were inserted into the bilayer in each conformation with its mass center ranging from the bilayer center to the bilayer-solvent boundary. These 103 conformations were used as the initial structure of each window. MD simulations were then carried out in the same fashion as previous P-binding and S-binding free energy calculations.

The window width, the force constant, and MD simulation protocols were the same in all of the PMF calculations. Weighted histogram analysis method (WHAM)<sup>33</sup> was employed in profile generation. The number of bins was 230, 90 and 250 for the P-binding PMF, the S-binding PMF, and the L-binding PMF, respectively.

**Data Analysis.** Protein backbone RMSDs with respect to the NMR structure (PDB: 2RLF) showed that the systems were equilibrated during the last 10 ns of the simulations (Fig. S3). Therefore, all data analyses for both the wild-type and the S31N mutant were done using this part of the simulation trajectories. Hydrogen bond (H-bond) was defined using a distance cutoff of 3.5 Å between the heavy atoms of the donor and the acceptor and an angle cutoff of 30° for  $\angle$  hydrogen-donor-acceptor. Hydrophobic interactions were considered to be formed if the distance between the mass centers of two hydrophobic groups is less than 6.5 Å based on the van der Waals potentials calculated using the GROMOS force field for alkyl groups (Fig. S9). At this cutoff distance, the pair-wise van der Waals potential energies between hydrophobic groups (carbon atoms) are around 0.2 kcal/mol. To monitor the change in orientation of rimantadine during the simulation, a vertical-axis and a horizontal-axis are defined in Fig. S1C and the respective results are shown in Figs. S5 and S7. The pore radius profiles are

calculated by two methods to evaluate the effects of rimantadine-binding on the M2 structure. In the first method, the average structure of the last 10 ns simulation was calculated using GROMACS and the pore radii along the channel helix were calculated using HOLE2<sup>34</sup> (Fig. S4). As the protein side chains might fluctuate among two or more alternative favorable conformations that the average structure may fail to capture, we also calculated pore radii for every snapshot in the simulation trajectory at a 10 ps interval for the last 10 ns. The average radii were then evaluated (Fig. 2). These two methods obtained similar pore radius profiles.

**pKa Estimation of Rimantadine in Different Environments.** The pKa values of rimantadine inside the P-binding site and the S-binding site were estimated by the PROPKA package.<sup>35, 36</sup> Five conformations were extracted from the last 10 ns simulation trajectory randomly for both binding sites. Each conformation was subject to pKa evaluation and the results were averaged and summarized in Table S1.

The estimated pKa values of rimantadine at the P-binding site and the S-binding site vary slightly from the value in solvent (10.4 according to Ref. 37). Nonetheless, at an environmental pH of 7.5 where the solution NMR structure was obtained, nearly all of the rimantadine species would be protonated for these two binding sites. As our study is focused on channel inhibition around neutral pH, we have used protonated rimantadine for all of the simulations.

**Helix Tilt Angle and Channel Tilt Angle Calculations.** Fig. S10 summarizes the tilt angle of each transmembrane alpha helix and the tilt angle of the helical bundle with respect to the membrane normal as a function of simulation time for all six structures in Table 2. The figure shows that the four helices do not have the same tilt angle, as the M2 channel has lost its C<sub>4</sub> symmetry during the simulation. In the wild-type, the tilt angle of one helix is about 35°; the angles of two other helices are about 25°; and the fourth helix has an angle of about 10°. In addition, the helix bundle is also tilted slightly (~15°) in the lipid bilayers. For the S31N mutant, three of the alpha helices have a tilt angle of about 23°, whereas the

fourth helix has a tilt angle of about 15°. The helix bundle is nearly perpendicular to the bilayer plane with little tilting in the mutant.

The results obtained in our simulation are in excellent agreement with Schweighofer et al.'s study that used similar simulation protocols,<sup>38, 39</sup> which verifies the accuracy and reliability of our simulation.

**Sensitivity of Free Energy Calculations to Force Fields.** To evaluate the effects of force field parameters on the accuracy of our description of proteins, we performed a second set of MD simulations and PMF calculations on the wild-type M2 channel using the OPLS all-atom force field to describe the protein and the rimantadine molecules as well as Berger's united-atom force field to describe the lipids. Such combination of force fields has been widely used in free energy calculations.<sup>40-44</sup> The "half- $\epsilon$  double-pairlist" combination method designed by Chris Neale and co-workers<sup>41, 42</sup> was used in our simulations.

The topology file for a rimantadine molecule in the OPLS all-atom force field was generated by the *Topolbuild* package ([http://www.gromacs.org/Downloads/User\\_contributions/Other\\_software](http://www.gromacs.org/Downloads/User_contributions/Other_software), access date: 05/02/11). The obtained atom types and partial charges are shown in Fig. S2C.

We calculated the P-binding PMF and the S-binding PMF of the wild-type M2 channel using the above-mentioned force fields (shown in Fig. S8). In this set of MD simulations and PMF calculations, we used nearly identical protocols as outlined in "Simulation Protocols" and "Potential of Mean Force Calculations", except for the change of force field that was used to describe the protein and the rimantadine molecules. A direct comparison between Figs. 3 and S8 would then provide valuable information on the effects of force fields on protein description. As Chew et al.<sup>29</sup> has found that the PMF of the lipid-binding state of adamantane drugs was not sensitive to the force field parameters on the drug molecules when Berger's united-atom force field was used to describe the lipids, we assume here that the lipid-binding state has the same free energy change as obtained in Fig. 3C.

From comparisons of Figs. 3 and S8, we can see that the PMFs of both the P-binding and the S-binding models are highly similar despite the change in force field for describing the protein and the rimantadine molecules. In particular, the energy barrier to reach the P-binding site from the N-terminal solvent using the OPLS all-atom force field is about 2 kcal/mol less than the barrier value obtained using the GROMOS united-atom force field for protein description. The energy well of the bound rimantadine-M2 complex in the P-binding model using the OPLS all-atom force field is about 4 kcal/mol more stable than the value obtained using the GROMOS united-atom force field. Similar magnitude of stability increase (~4 kcal/mol) is found for the S-binding model using the OPLS all-atom force field. These energy results are summarized in Table S3.

In summary, despite the slight differences in the calculated free energy values shown in Figs. 3 and S8, the same conclusion can be reached, which is that the P-binding model is the more thermodynamically-favored drug-binding site (about 7 kcal/mol more stable than the S-binding model), whereas the S-binding model may be more accessible under kinetic binding conditions.



## References:

- (1) Chizhnikov, I. V.; Geraghty, F. M.; Ogden, D. C.; Hayhurst, A.; Antoniou, M.; Hay, A. J. *J. Physiol.* **1996**, *494*, 329-336.
- (2) Pinto, L. H.; Lamb, R. A. *Photochem. Photobiol. Sci.* **2006**, *5*, 629-632.
- (3) Pinto, L. H.; Lamb, R. A. *J. Biol. Chem.* **2006**, *281*, 8997-9000.
- (4) Stouffer, A. L.; Acharya, R.; Salom, D.; Levine, A. S.; Di Costanzo, L.; Soto, C. S.; Tereshko, V.; Nanda, V.; Stayrook, S.; DeGrado, W. F. *Nature* **2008**, *451*, 596-599.
- (5) Schnell, J. R.; Chou, J. J. *Nature* **2008**, *451*, 591-595.
- (6) Luo, W.; Mani, R.; Hong, M. *J. Phys. Chem. B* **2007**, *111*, 10825-10832.
- (7) Hu, J.; Asbury, T.; Achuthan, S.; Li, C.; Bertram, R.; Quine, J. R.; Fu, R.; Cross, T. A. *Biophys. J.* **2007**, *92*, 4335-4343.
- (8) Sansom, M. S. P.; Kerr, I. D.; Smith, G. R.; Son, H. S. *Viol.* **1997**, *233*, 163-173.
- (9) Pinto, L. H.; Dieckmann, G. R.; Gandhi, C. S.; Papworth, C. G.; Braman, J.; Shaughnessy, M. A.; Lear, J. D.; Lamb, R. A.; DeGrado, W. F. *Proc. Natl. Acad. Sci. USA* **1997**, *94*, 11301-11306.
- (10) Sharma, M.; Yi, M.; Dong, H.; Qin, H.; Peterson, E.; Busath, D. D.; Zhou, H. X.; Cross, T. A. *Science* **2010**, *330*, 509-511.
- (11) Hu, F.; Luo, W.; Hong, M. *Science* **2010**, *330*, 505-508.
- (12) Kass, I.; Arkin, I. T. *Structure* **2005**, *13*, 1789-1798.
- (13) Jing, X.; Ma, C.; Ohigashi, Y.; Oliveira, F. A.; Jardetzky, T. S.; Pinto, L. H.; Lamb, R. A. *Proc. Natl. Acad. Sci. USA* **2008**, *105*, 10967-10972.
- (14) Wang, C.; Takeuchi, K.; Pinto, L. H.; Lamb, R. A. *J. Virol.* **1993**, *67*, 5585-5594.
- (15) Duff, K. C.; Gilchrist, P. J.; Saxena, A. M.; Bradshaw, J. P. *Viol.* **1994**, *202*, 287-293.
- (16) Balannik, V.; Carnevale, V.; Fiorin, G.; Levine, B. G.; Lamb, R. A.; Klein, M. L.; DeGrado, W. F.; Pinto, L. H. *Biochem.* **2010**, *49*, 696-708.

- (17) Balannik, V.; Wang, J.; Ohigashi, Y.; Jing, X.; Magavern, E.; Lamb, R. A.; DeGrado, W. F.; Pinto, L. H. *Biochem.* **2009**, *48*, 11872-11882.
- (18) Ohigashi, Y.; Ma, C.; Jing, X.; Balannick, V.; Pinto, L. H.; Lamb, R. A. *Proc. Natl. Acad. Sci. USA* **2009**, *106*, 18775-18779.
- (19) Pielak, R. M.; Schnell, J. R.; Chou, J. J. *Proc. Natl. Acad. Sci. USA* **2009**, *106*, 7379-7384.
- (20) Berendsen, H. J. C.; van der Spoel, D.; Van Drunen, R. *Comput. Phys. Commun.* **1995**, *91*, 43-56.
- (21) Lindahl, E.; Hess, B.; van der Spoel, D. *J. Mol. Model.* **2001**, *7*, 306-317.
- (22) Berger, O.; Edholm, O.; Jahnig, F. *Biophys. J.* **1997**, *72*, 2002-2013.
- (23) Schuttelkopf, A. W.; van Aalten, D. M. F. *Acta. Crystallogr., D Biol. Crystallogr.* **2004**, *60*, 1355-1363.
- (24) Psachoulia, E.; Sansom, M. S. P. *Biochem.* **2008**, *47*, 4211-4220.
- (25) Gordon, J. C.; Myers, J. B.; Folta, T.; Shoja, V.; Heath, L. S.; Onufriev, A. *Nucleic Acids Res.* **2005**, *33*, 68-71.
- (26) Anandakrishnan, R.; Onufriev, A. *J. Comput. Biol.* **2008**, *15*, 165-184.
- (27) Chen, H.; Wu, Y.; Voth, G. A. *Biophys. J.* **2007**, *93*, 3470-3479.
- (28) Hess, B.; Bekker, H.; Berendsen, H. J. C.; Fraaije, J. G. E. M. *J. Comput. Chem.* **1997**, *18*, 1463-1472.
- (29) Chew, C. F.; Guy, A.; Biggin, P. C. *Biophys. J.* **2008**, *95*, 5627-5636.
- (30) Torrie, G. M.; Valleau, J. P. *J. Comp. Phys.* **1977**, *23*, 187-199.
- (31) Patra, M.; Karttunen, M.; Hyv nen, M. T.; Falck, E.; Lindqvist, P.; Vattulainen, I. *Biophys. J.* **2003**, *84*, 3636-3645.
- (32) Patra, M.; Karttunen, M.; Hyv nen, M. T.; Falck, E.; Vattulainen, I. *J. Phys. Chem. B* **2004**, *108*, 4485-4494.
- (33) Kumar, S.; Rosenberg, J. M.; Bouzida, D.; Swendsen, R. H.; Kollman, P. A. *J. Comput. Chem.* **1992**, *13*, 1011-1021.

- (34) Smart, O. S.; Neduvelil, J. G.; Wang, X.; Wallace, B. A.; Sansom, M. S. P. *J. Mol. Graphics.* **1996**, *14*, 354-360.
- (35) Li, H.; Robertson, A. D.; Jensen, J. H. *Proteins: Struct., Funct., Bioinf.* **2005**, *61*, 704-721.
- (36) Bas, D. C.; Rogers, D. M.; Jensen, J. H. *Proteins: Struct., Funct., Bioinf.* **2008**, *73*, 765-783.
- (37) Spector, R. *J. Pharmacol. Exp. Ther.* **1988**, *244*, 516-519.
- (38) Carpenter, T.; Bond, P. J.; Khalid, S.; Sansom, M. S. P. *Biophys. J.* **2008**, *95*, 3790-3801.
- (39) Schweighofer, K. J.; Pohorille, A. *Biophys. J.* **2000**, *78*, 150-163.
- (40) Tieleman, D. P.; MacCallum, J. L.; Ash, W. L.; Kandt, C.; Xu, Z.; Monticelli, L. *J. Phys.: Condens. Matter* **2006**, *18*, 1221-1234.
- (41) Chakrabarti, N.; Neale, C.; Payandeh, J.; Pai, E. F.; Pomès, R. *Biophys. J.* **2010**, *98*, 784-792.
- (42) Cuesta-Seijo, J. A.; Neale, C.; Khan, M. A.; Moktar, J.; Tran, C. D.; Bishop, R. E.; Pomès, R.; Privé, G. G. *Structure* **2010**, *18*, 1210-1219.
- (43) Bjelkmar, P.; Niemel, P. S.; Vattulainen, I.; Lindahl, E. *PLoS Comput. Biol.* **2009**, *5*.
- (44) Ramachandran, S.; Serohijos, A. W. R.; Xu, L.; Meissner, G.; Dokholyan, N. V. *PLoS Comput. Biol.* **2009**, *5*.

**Table S1.** The estimated pKa values of rimantadine molecules at different binding sites as well as the corresponding percentages of protonated rimantadine with respect to all states of rimantadine at pH 7.5. In the acid-base equilibrium of rimantadine,  $\text{HA}^+ \rightarrow \text{H}^+ + \text{A}$ ,  $\text{HA}^+$  represents protonated rimantadine and A represents deprotonated rimantadine. The protonation percentage is defined as  $100\% [\text{HA}^+] / ([\text{A}] + [\text{HA}^+])$ . For the S-binding sites where four rimantadine molecules are bound, four different pKa values are shown.

		Wild-type				S31N mutant			
P-binding site	pKa	$9.0 \pm 0.4$				$8.6 \pm 0.1$			
	Protonation percentage	97%				93%			
S-binding site	Rimantadine molecule	1	2	3	4	1	2	3	4
	pKa	$12.9 \pm 0.1$	$12.6 \pm 0.3$	$10.0 \pm 0.1$	$12.3 \pm 0.2$	$13.3 \pm 0.5$	$12.6 \pm 0.5$	$10.0 \pm 0.2$	$10.0 \pm 0.1$
	Protonation percentage	>99%	>99%	>99%	>99%	>99%	>99%	>99%	>99%

**Table S2.** Percentage of time that hydrophobic interactions were observed between S-binding site rimantadine molecules and the side chains of Leu40, Ile42 and Leu43 of the M2 channel during the molecular dynamics simulations. The distances between the center of mass of the adamantane group of rimantadine and the centers of mass of the side chains were calculated for each snapshot in the simulation trajectory, and those shorter than 6.5 Å (Fig. S9) were counted and summarized here.

Wild-type	1	2	3	4
Leu40	100%	79%	100%	70%
Ile42*	23%	97%	63%	0
Leu43	75%	98%	17%	64%
S31N mutant	1	2	3	4
Leu40	99%	43%	90%	0
Ile42	82%	0	27%	0
Leu43	25%	33%	0	0

\* Each rimantadine molecule forms hydrophobic interactions with Leu40 and Leu43 from one M2 peptide and Ile42 from the adjacent peptide.

**Table S3.** Comparison of free energy values (in kcal/mol) obtained from two sets of PMF calculations. In the first set of PMF calculations (“Potential of Mean Force Calculations” section and Fig. 3), the GROMOS united-atom force field was used for describing the protein and the rimantadine molecules. In the second set of PMF calculations (“Sensitivity of Free Energy Calculations to Force Fields” section and Fig. S8), the protein and the rimantadine molecules were described by the OPLS all-atom force field. In both PMF calculations, Berger’s united-atom force field was used for lipids.

Description of the protein and the rimantadine molecules	GROMOS united-atom force field		OPLS all-atom force field	
	P-binding	S-binding	P-binding	S-binding
Energy barrier from the solvent-bound state	10	0	8	0
Depth of the energy well	-18	-2	-22	-6
Free energy change from the solvent-bound state	-18	-11	-22	-15
Free energy change from the L-binding state	-9	-2	-13	-6

**Fig. S1. Molecules used in the simulation.** (A) The protein sequence of the M2 channel used in this study. The transmembrane helix contains 22 residues. The hydrophobic residues are colored in blue, polar residues in green, residues with charge in red and glycine in black. Pore-lining residues in the solution NMR structure are in bold-face. (B) A schematic diagram showing our simulation system. The lipid molecules are shown in the line representation, the protein in the ribbon form, and water as gray space-filling spheres. (C) Structure of the protonated rimantadine used in the simulation. Atoms C1 and C2 define the vertical-axis, whereas the projection of the line connecting C3 and the nitrogen atom onto the X-Y plane of the simulation system is defined as the horizontal-axis (Z being the channel helix and membrane normal).

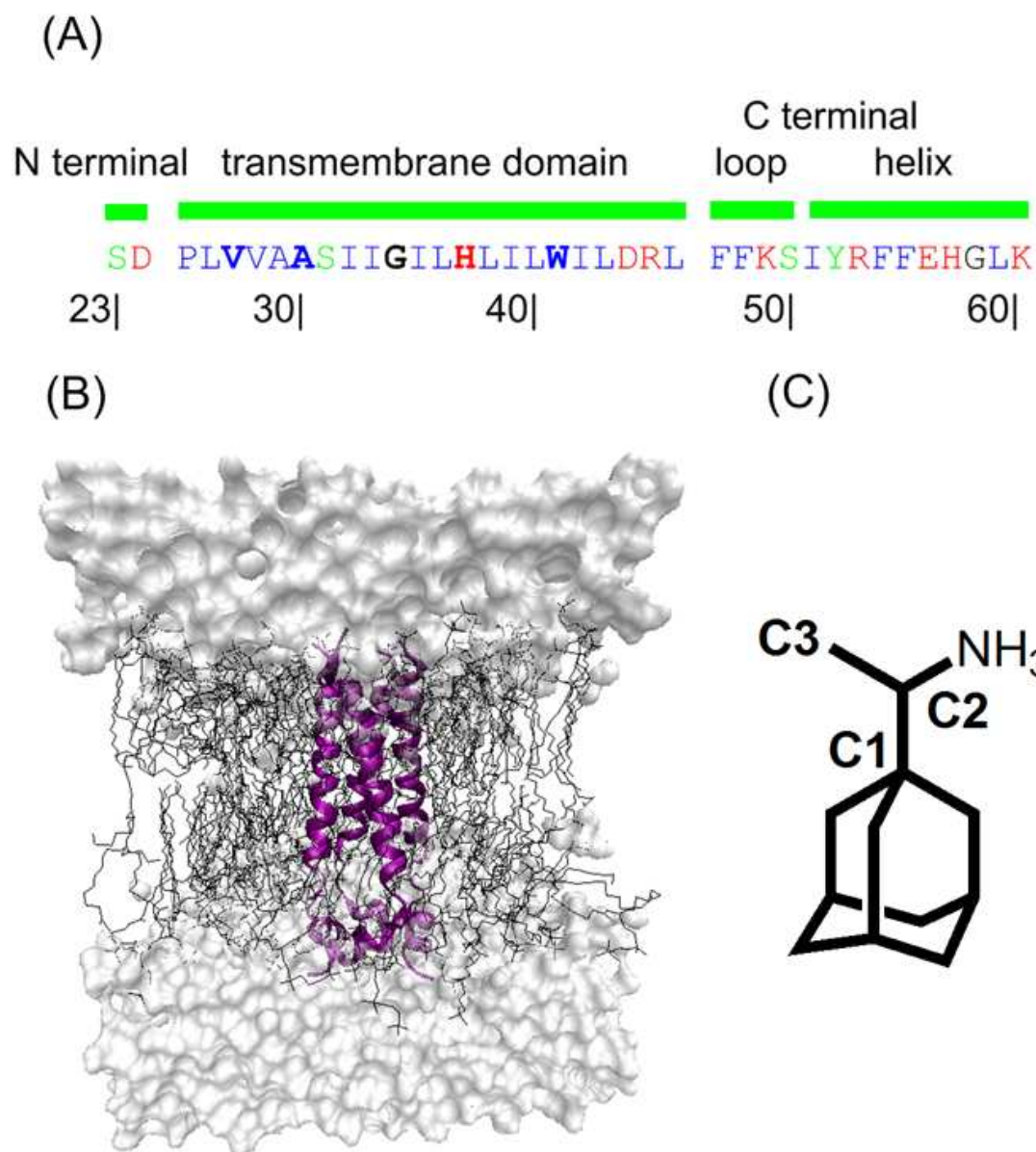






**Fig. S3.** The backbone RMSD of the six simulated structures in Table 2 during molecular dynamics simulations. For all simulations, the RMSD values plateau at about 3 Å after about 4-5 ns, indicating the equilibration of the simulated systems.

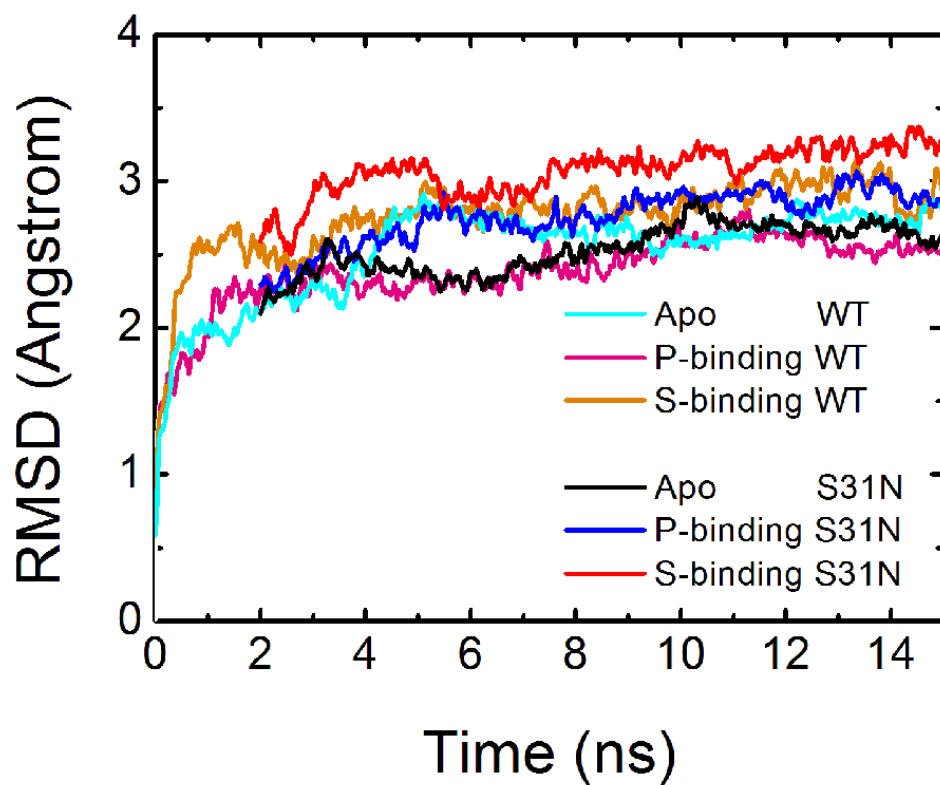


**Fig. S4. Pore diameters calculated by HOLE2 for the average structure of M2 channel during the last 10 ns simulation for each structure in Table 2.** The region of the pore surface colored in red is too narrow to accommodate a water molecule whose radius is about 1.4 Å. The green region represents portions of the channel that is large enough to accommodate one water molecule. The blue region can accommodate two or more water molecules. It can be seen that the P-binding form has the largest pore radii among all 3 forms and the S31N mutation caused the N-terminal channel pore to be enlarged.

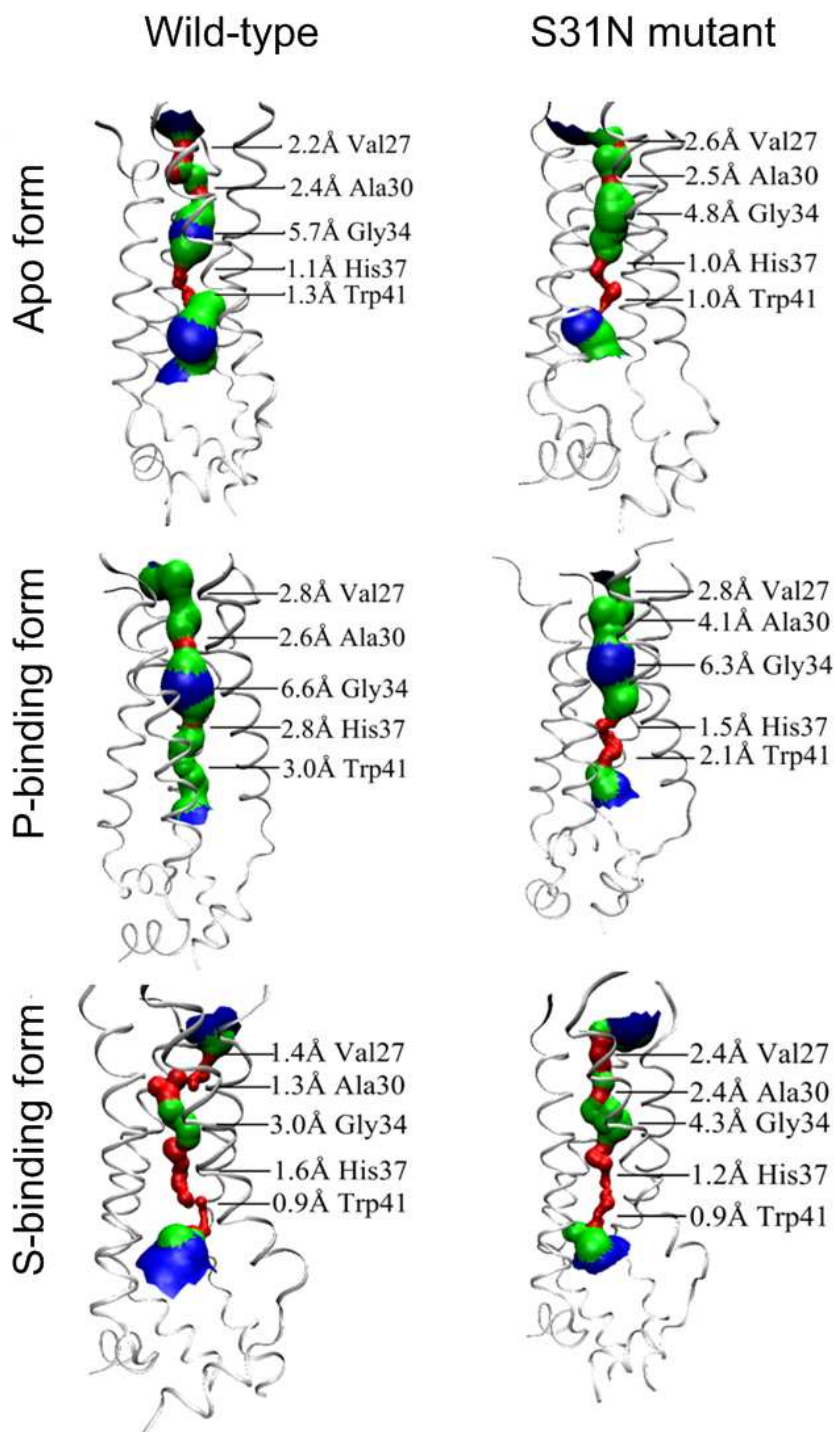


**Fig. S5. The orientation and rotation of rimantadine in the P-binding model of the wild type (the upper panel) and the S31N mutant (the lower panel).** The tilt angle between the vertical-axis (defined in Fig. S1C) of rimantadine and the channel helix is plotted on the left (black) with its distribution (red); the angle between the horizontal-axis (defined in Fig. S1C) of rimantadine and its starting orientation on the X-Y plane of the simulation system is plotted on the right.

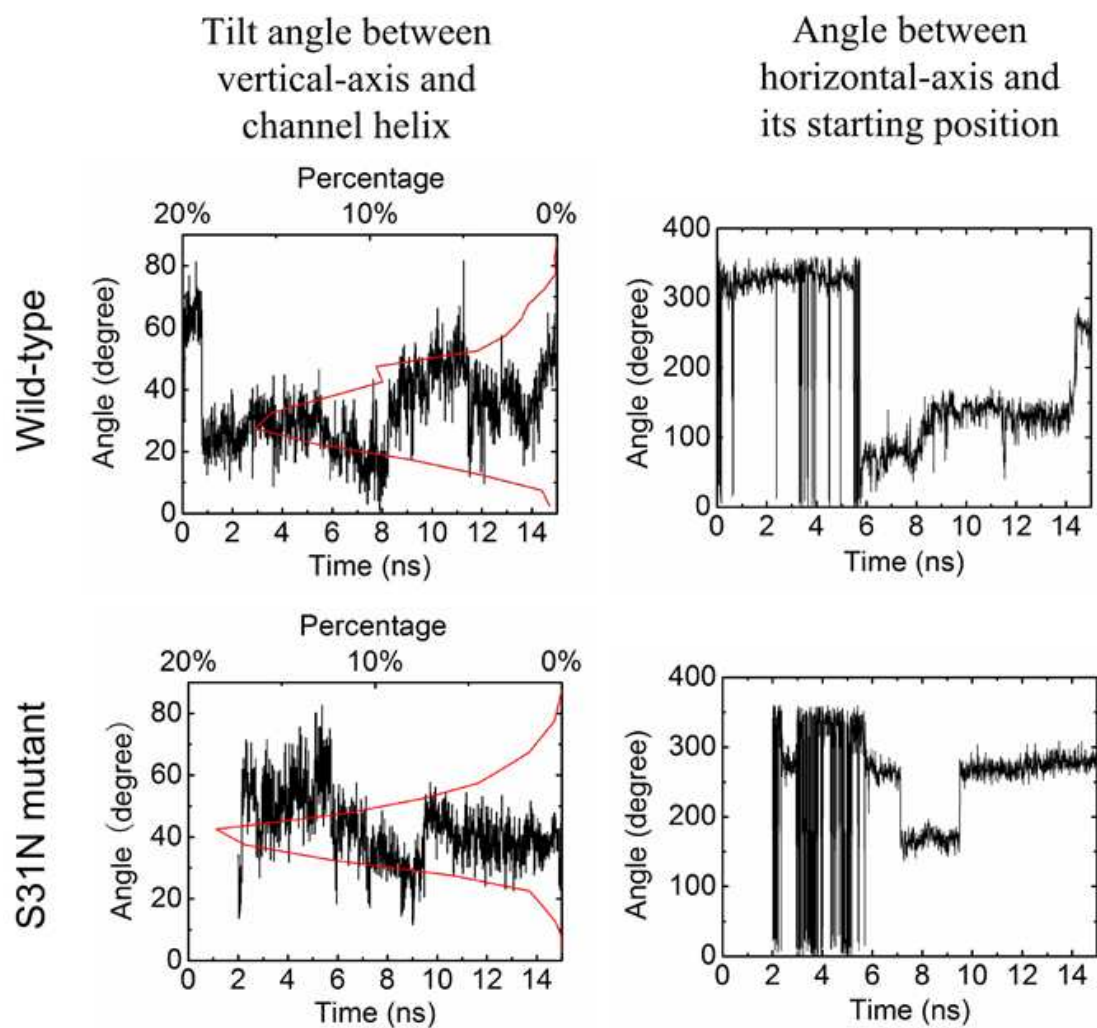


**Fig. S6. Snapshots of the P-binding rimantadine molecule during the MD simulation.** The drug molecule is observed to be rotating around its vertical axis defined in Fig. S1C.

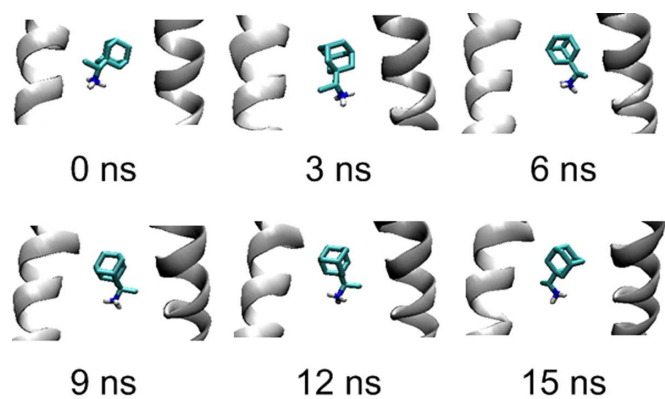


**Fig. S7. The orientation of the four rimantadine molecules in the S-binding model of (A) the wild type and (B) the S31N mutant.** The tilt angle (black) between the vertical-axis (defined in Fig. S1C) of each rimantadine molecule and the channel helix is plotted with its distribution (red).

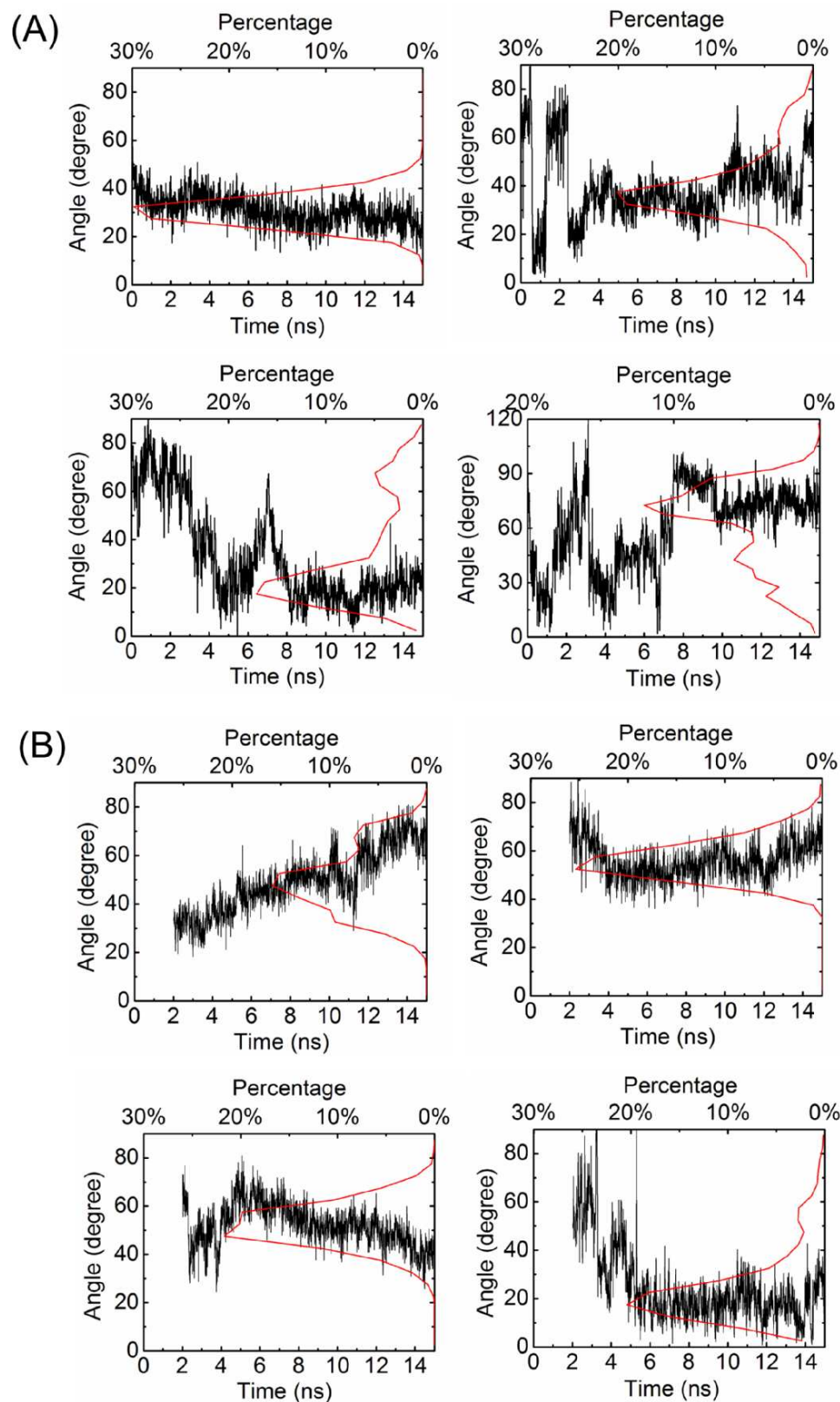


**Fig. S8. The potential of mean force (PMF) profiles for the P-binding and the S-binding sites in the wild-type M2-lipid environment.** The OPLS all-atom force field was used for describing the M2 protein and the rimantadine molecules, whereas the Berger's united-atom force field was used for describing lipids. Panel A shows the pore-binding PMF of a rimantadine molecule entering the channel pore from the N-terminal end. Panel B shows the PMF of a rimantadine molecule leaving the surface-binding site and entering the lipid-water environment. The shaded region in panel A represents the lipid-water interface where both water molecules and lipid head groups are present. The protein-lipid interface as well as the lipid region are labeled in panel B.

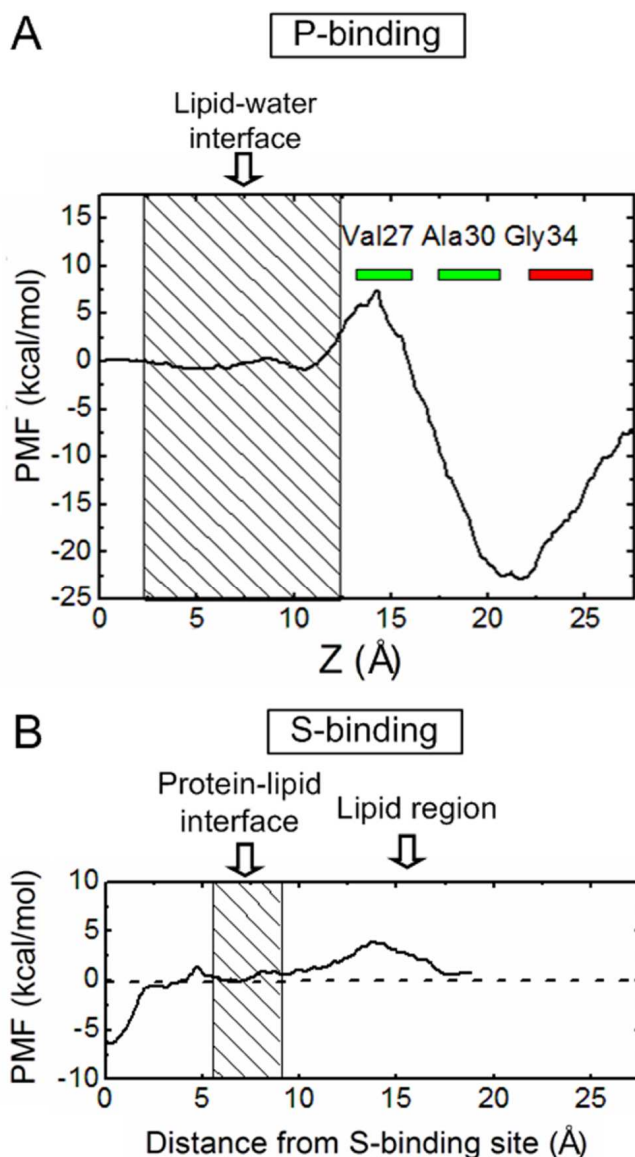


**Fig. S9. The pair-wise Lennard-Jones van der Waals potential energies between different atom types based on the GROMOS united-atom force field.** Based on this plot, hydrophobic interactions are considered to exist among hydrophobic groups that are within 6.5 Å.

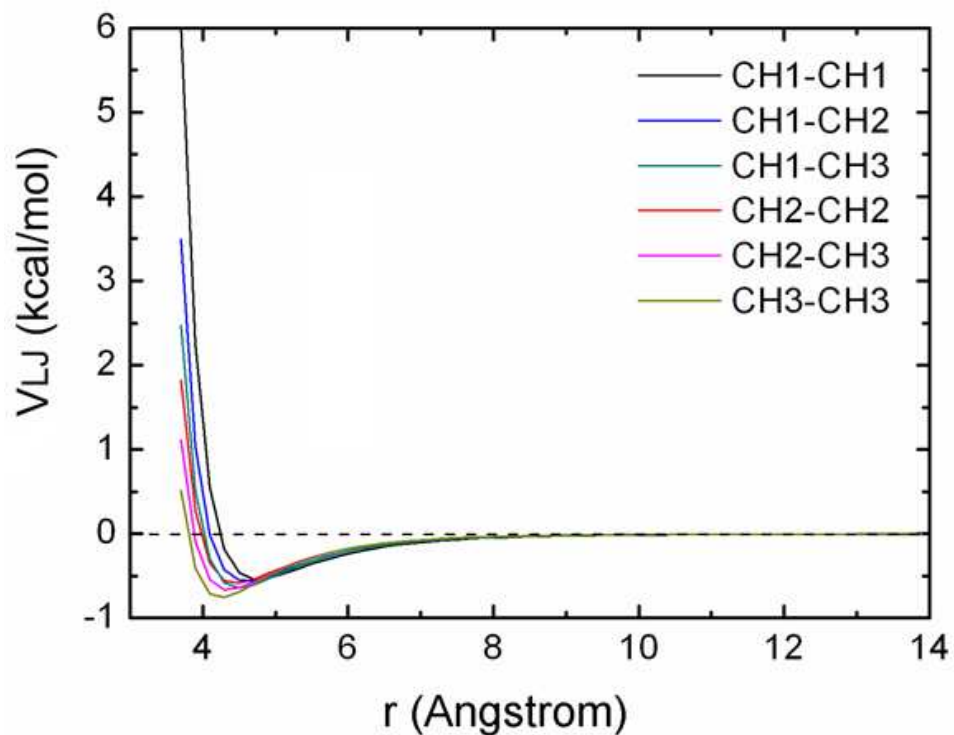




**Fig. S10. Tilt angle of each M2 transmembrane helix as well as the M2 helix bundle for the structures in Table 2 as a function of simulation time.** The left column is for the wild type protein whereas the right column is for the S31N mutant. The top, middle, and bottom rows are for the apo-form, the P-binding form, and the S-binding form, respectively. The tilt angle of the entire helix bundle is shown in black. The tilt angles of the four transmembrane helices are shown in red, green, blue and cyan, respectively.

